RSC Advances

RSC Publishing

PAPER

View Article Online
View Journal | View Issue

Simulation and modelling of sub-30 nm polymeric channels fabricated by electrostatic induced lithography

Cite this: *RSC Advances*, 2013, **3**, 11839

H. Li,[ab] W. Yu,*[a] L. Zhang,[a] Z. Liu,[a] K. E. Brown,[c] E. Abraham,[c] S. Cargill,[c] C. Tonry,[d] M. K. Patel,[d] C. Bailey[d] and M. P. Y. Desmulliez*[c]

Received 14th January 2013,
Accepted 26th April 2013

DOI: 10.1039/c3ra40188j

www.rsc.org/advances

This article demonstrates, through finite element analysis, the possibility to manufacture sub-30 nm polymeric channels using electrostatic induced lithography. Channels with a width of 25 nm, a depth of 50 nm and an inter-channel wall of 28 nm can be obtained by this patterning process. The influence of operational parameters such as the filling factor, the aspect ratio of the master electrode, the applied voltage and the gap between the two electrodes and initial film thickness has been studied in detail to define the fabrication limits of this process in the case of periodic nanostructures. Conclusions for such nanostructures can be generalised to other shapes manufactured from polymers.

Introduction

Nanopatterning of surfaces is witnessing increasing interest from scientists and engineers for applications ranging from microelectronics, biomaterials and micro/nanofluidic devices to photonic crystals. In that regard, scientists have turned to unusual patterning techniques to engineer surfaces that are not easily manufacturable by conventional lithographic methods. Among them the two most representative methods are dewetting[1–7] and electrohydrodynamic instability patterning (EHDIP).[8–39] In the former case, liquid polymeric films subjected to a long range van der Waals force produce an array of droplets on polished rigid substrates. The mechanism behind this phenomenon can be either spinodal dewetting or heterogeneous nucleation. A physically or chemically induced change in the properties of the substrate can effectively control the order and morphology of these self-organized induced microstructures. In the latter case, electrohydrodynamic instabilities on the interface of a thin polymer film have the potential to create nanoscale structures. This patterning method exploits the instability of a polymeric film under the influence of a heterogeneous electric field.

[a]*State Key Laboratory of Applied Optics, Changchun Institute of Optics, Fine Mechanics & Physics, Chinese Academy of Sciences, No.3888, Dongnanhu Road, Changchun, Jilin, P.R.China. E-mail: yuwx@ciomp.ac.cn; Fax: +86 0431 86176058; Tel: +86 0431 86176058*

[b]*University of Chinese Academy of Sciences, Beijing, 100049, P.R. China*

[c]*MIcroSystems Engineering Centre (MISEC), School of Engineering & Physical Sciences, Heriot-Watt University, Edinburgh EH14 4AS, UK. E-mail: m.desmulliez@hw.ac.uk; Fax: +44 (0)131 451 4155; Tel: +44 (0)131 451 3340*

[d]*School of Computing and Mathematical Sciences, University of Greenwich, Old Royal Naval College, Park Row, London SE10 9LS, UK*

Scientists have long derived theoretically the destabilizing effect of electric forces on the free surface of a film.[8–13] Similar research was carried out to describe the time evolution of the instability of the interface between thin fluid films subjected to an electric field.[14–16] Chou and coworkers were first to correlate the instability of the film and the resulting pattern formation. In observing that the viscous polymer film could spontaneously form pillars when subjected to an external, vertical electric field they named this phenomenon lithographically induced self assembly (LISA).[17] Almost at the same time, Schäffer found that electrohydrodynamic instabilities could form well-defined pillars.[18,19] An array of hexagonal columns was found to be the most dominant morphology formed for a spatially homogeneous electric field. Since EHDIP could usefully be applied to enhance electronic devices, sensors, optical band gap crystals or biochips, numerous theoretical and experimental works have been done to understand this phenomenon.[20–37]

Theoretical studies have largely been based on linear stability analysis, which is only applicable to the early stage of the evolution of the interface. As the amplitude of the perturbations grows larger, the phenomenon can be only explained properly by weekly nonlinear stability analysis[36,37] and the dynamic evolution of the interface growth should only be modelled by a nonlinear simulation.[37–39] A lot of simulations demonstrate that under a featureless mask the final morphology contains arrays of hexagonal columns, a result which is in agreement with weakly nonlinear analysis.[36] The order of the final hexagonal pattern largely depends on the thickness ratio ξ relating the air gap to the film thickness. However, under patterned masks, well-ordered polymeric micro- and nanostructures can be obtained over large

areas.[18,40] Moreover, the formed structures can be a replica of the pattern of the mask, enabling thereby the possibility of manufacturing surfaces on the nanoscale. Because of the pattern of the mask, the field is heterogeneous and the stable state is no longer time independent, which renders the linear stability and nonlinear stability analyses difficult to implement. Numerical simulation is therefore used in this article to describe the dynamic evolution of the interface under these conditions. The final morphology of the micro/nanostructured pattern in the thin film is determined by the competitive behaviour of the applied gradient flow on account of the heterogeneity of the electric field and the spinodal flow due to the local thickness variation. By using a qualitative analysis method, Verma gave the ideal conditions necessary for ideal replication and indicated that the number density of the electric field induced patterns can be altered by varying the applied voltage or tuning the mean film thickness, periodicity, and depth of grooves on the top electrode.[38] The study on numerical simulations tracing nonlinear free surface deformations using a finite element computational methodology was carried out by Hak Koon Yeoh[43] and Qingzhen Yang.[44] In the former work, the evolution of the interface shapes with an increasing nonuniformity of the applied electric field and the limits of stability of thin films subjected to nonuniform electric fields are described. In the latter work, a numerical model is built to find out the critical values of the parameters that induce the stability of the polymeric film produced by the EHDIP method and is compared with other models.

To date, there has been no article reporting how to define the period limit L_P, *i.e.* the fabrication limit of the periodic nanostructures using finite element analysis. This paper is dedicated to finding how important operational parameters affect the period limit L_P. Three methods can usually be used to create smaller features: the surface tension can be decreased either by changing the polymer material or modifying the surface properties, or the electrostatic stress and spatially heterogeneous electric field can be increased. This article is focused on the third method, which involves modelling the change of the structures of the grating mask.[41] The numerical simulation method based on the finite element analysis method is employed to investigate the influence on L_P of the filling factor, the aspect ratio, the initial mean film thickness, the electrode spacing and the applied voltage between the two electrodes. These results are paramount to the design, optimization and fabrication of nanochannels for practical applications.

Simulation model and methods

The schematic drawing of the experimental setup is sketched in Fig. 1. The polymer film, considered here to be an isothermal and perfect dielectric fluid, is confined between either two flat electrodes as shown in Fig. 1(a), or a periodically patterned electrode and a flat electrode as shown in Fig. 1(b). The initial film thickness is h_0. When the film is perturbed by

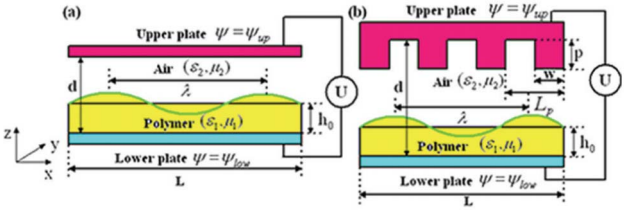

Fig. 1 Schematic diagrams of thin films resting on rigid substrates subjected to an external (a) homogeneous electric field and (b) heterogeneous electric field.

an infinitesimal disturbance, the local film thickness is denoted by $h(x,y)$ in Cartesian coordinates, where (x,y) are the coordinates along the plane of the electrode. We will assume that the electrodes are infinitely long such that h is only a function of x. The polymeric film is assumed here to be surrounded by air. The viscosity and permittivity of the two fluids are denoted by μ_i and ε_i, respectively and considered to be space-independent. The subscript i is used to distinguish the fluid phase: $i = 1$ for the film and $i = 2$ for the air. The mask with the voltage ψ_{up} is positioned above the lower electrode with the voltage ψ_{low} at a distance d. For a patterned mask, the height of the electrode protrusions, the width of the electrode protrusions, and the period of the grating mask are denoted by p, w and l, respectively.

Numerous theoretical and experimental studies have been devoted to the physical mechanism of electrohydrodynamic instabilities, which induce a wave pattern with a characteristic wavelength λ.[38–41] The viscous polymer film, which is assumed to be a perfect dielectric medium is subject to the electrostatic pressure exerted by the externally applied electric field at the film–air interface. In order to simplify the analytic equation, we will assume here that the electric field is perpendicular to the surface of the fluid. The high electric field generates sufficient electrostatic forces at the interface to overcome the surface tension and destabilizes the thin liquid film. Because of the presence of these fluctuations, wave crests and troughs in the film experience slightly different electrostatic stress strengths, producing thereby a pressure-driven Poiseuille flow. The crests of the film experience a larger electrostatic stress than the troughs, such that the total pressure at the wave crests is smaller, leading the film to flow from the troughs to the crests as shown in Fig. 1. A topographically patterned electrode can lead to a periodically modulated field as shown in Fig. 1(b). The emerging structures in the film are then driven towards the salient features of the master, which protrude downward towards the polymer film where the electrostatic force is the strongest. Under appropriate conditions, the polymer can replicate the master pattern, inducing well-defined channels. In the long wave limit,[42] the total pressure at the interface, p, is given by:[19]

$$p = p_0 - \zeta \frac{\partial^2 h}{\partial x^2} + p_{el}(h) + p_{dis}(h) \quad (1)$$

where p_0 is the atmospheric pressure, ζ is the interfacial

tension parameter, p_{el} is the electrostatic pressure and p_{dis} is the disjoining pressure. The Laplace pressure given by the second term plays an important role in maintaining the stability of the film. The electrostatic pressure can be described by the following equation:[38]

$$p_{el} = -0.5\varepsilon_0\varepsilon_p(\varepsilon_p - 1)E_p^2 \quad (2)$$

$$E_p = \frac{U}{\varepsilon_p d - (\varepsilon_p - 1)h} \quad (3)$$

where E_p is the electric field strength in the polymer film, and U is the electrical potential applied between the upper electrode and the lower electrode. In general, the disjoining and atmospheric pressures are negligible compared to the electrostatic pressure. For the selection of the modes, linear stability analysis is used to predict the characteristic wavelength. A small sinusoidal perturbation of the interface with wave vector q, growth rate $1/\tau$, and amplitude u is considered:

$$h(x,t) = h_0 + ue^{iqx + t/\tau} \quad (4)$$

which is substituted into the equation describing the evolution of the free surface,

$$\frac{\partial h}{\partial t} = \frac{\partial}{\partial x}\left[\frac{h^3}{3\mu}\left(\frac{\partial p}{\partial x}\right)\right] \quad (5)$$

The resulting linear dispersion relation is:

$$\tau^{-1} = -\frac{{h_0}^3}{3\mu}\left(\zeta q^4 + \frac{\partial p_{el}(h)}{\partial h}q^2\right) \quad (6)$$

The dominant wavelength λ, of the fastest growing linear mode is given by:

$$\lambda = 2\pi\sqrt{\frac{2\zeta U}{\varepsilon_0\varepsilon_p(\varepsilon_p - 1)^2}}E_p^{-3/2} \quad (7)$$

In this article, a model in COMSOL MULTIPHYSICS (Version 4.3, COMSOL group) has been developed to look at the evolution of the structure due to the electrostatic force and surface tension at the interface of the liquid polymer. The interface between the immiscible polymer film and air phases is tracked by using a level set method, where the phase is characterized by a level set function ϕ. For this model the liquid, which is considered as a perfect dielectric medium and incompressible medium, obeys the incompressible Navier–Stokes equations. The laminar, level set method for the two phase-flow module and the electrostatics module were also employed to deal with the surface tension force of the fluid as well as the electrostatic pressure acting on the surface of the fluid respectively.[45,46] In the model, four periods of instabilities are considered and the periodic boundary condition is applied at boundaries 1, 3, 22, and 23 as shown in Fig. 2.

The geometry and mesh of the model are presented in the same figure. A DC voltage of 50 V is applied between the bottom (boundary 2) and the top electrode (boundaries 5, 6, 7...19, 20 and 21). The boundary conditions for the fluid flow are: (a) no slip at boundaries 2, 5, 6, 7...19, 20 and 21; (b) periodic boundary on boundaries 1, 3, 22 and 23; (c) initial fluid interface at boundary 4; (d) pressure point constraint applied at points a and b, namely, the two ends of the air–film interface. In order to get a large area of the periodic structure, it is necessary to introduce the periodic boundary conditions at boundaries 1, 3, 22 and 23, with sources 1 and 3 corresponding to destinations 23 and 22, respectively. The expressions for the sources are P, the pressure in the fluid, and $\boldsymbol{U}$, the flow velocity. The two-phase flow is in the form of the conservative level set. The properties of the polymer liquid used in the simulation are presented in Table 1.

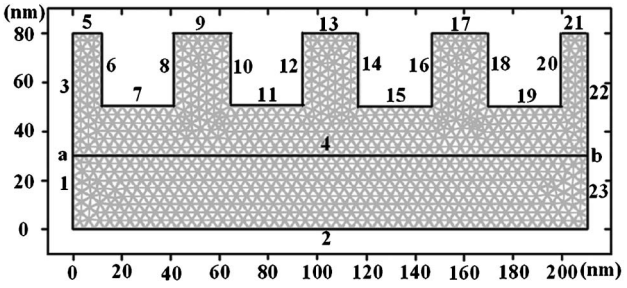

Fig. 2 A schematic diagram introducing the geometry, boundary conditions and mesh of the two-dimension model. Dimension unit is nm.

A high electric field generates sufficient electrostatic forces on the interface to overcome the surface tension, and destabilizes the thin liquid film so that the polymer fluid is pulled towards the protrusion of the top electrode. The film and the air are assumed to be perfect dielectric media with zero net charge in the bulk. Both assumptions give rise to the equations governing the force exerted on the interface. The electric field is solved using the Laplace equation for the voltage assuming that there is zero free charge in the bulk fluid:

$$\nabla\cdot(\varepsilon_0\varepsilon_r\nabla V) = 0 \quad (8)$$

Where ε_0 is the dielectric permittivity of the vacuum, ε_r is the dielectric constant of the air or polymer, and V is the voltage. $\varepsilon_r = 1 + 1.5\phi$, where $\phi = 0$ or 1 and denotes the air or polymer, respectively. The interface is given by the contour of the level function $\phi = 0.5$. The velocity and pressure field of the two-phase flow are governed by the incompressible Navier–Stokes and continuity equations:

$$\rho\frac{\partial \boldsymbol{U}}{\partial t} + \rho(\boldsymbol{U}\cdot\nabla)\boldsymbol{U} = -\nabla p + \nabla\cdot(\mu\nabla\boldsymbol{U}) + \boldsymbol{F} \quad (9)$$

$$\frac{\partial \rho}{\partial t} + \nabla\cdot(\rho\boldsymbol{U}) = 0 \quad (10)$$

$$\rho = \rho_1 + (\rho_2 - \rho_1)\phi \quad (11)$$

Table 1 The properties of the material used in the numerical simulations

Simulated dynamic viscosity (Pa s)	Density (kg m^{-3})	Dielectric constant	Surface tension (N m^{-1})
1	1000	2.5	0.038

$$\mu = \mu_1 + (\mu_2 - \mu_1)\phi \tag{12}$$

The level set function smooths the density and viscosity jump across the interface. In the equations above, ρ_1 and ρ_2 are the fluid densities of the air and polymer film, μ_1 and μ_2 indicate the dynamic viscosities of the air and the polymer film, U is the flow velocity, t represents time and p is the pressure. $\boldsymbol{F}$ is the volume force caused by the atmospheric pressure p_0, the surface tension $\boldsymbol{F}_{st} = \sigma\kappa\delta n$, and the electrostatic pressure p_{el}, and is denoted by $\boldsymbol{F} = (p_0 + \sigma\kappa + p_{el})\delta\boldsymbol{n}$, where σ is the surface tension, κ is the curvature, δ is a delta function concentrated at the surface, and $\boldsymbol{n}$ is the unit outward normal to the interface.

The transport of the interface can be tracked by solving the equation

$$\frac{\partial\phi}{\partial t} + \boldsymbol{U}\cdot\nabla\phi = \gamma\nabla\cdot(\varepsilon\nabla\phi - \phi(1-\phi)\frac{\nabla\phi}{|\nabla\phi|}) \tag{13}$$

where γ determines the amount of reinitialization of the level set function and the parameter ε determines the thickness of the interface. A suitable value for γ is the maximum magnitude of the velocity field in the model and $\varepsilon = h_c/2$, where h_c is the characteristic mesh size in the region passed by the interface. In our simulation, $\gamma = 0.1$ and ε is $\sqrt{2.5}$.

Results and discussions

As shown in Fig. 3(a), the top electrode with a one-dimensional periodic nanostructure is used as a master to fabricate the nanochannels in the polymer. The period for the nanostructure is 53 nm, the width and the height of the electrode protrusions are both 30 nm, the initial film thickness of the polymer is 30 nm, the applied voltage is 50 V and the air gap between the bottom of the electrode protrusions and the polymer surface is 20 nm. As the spatial heterogeneity of the electrostatic field is generated by the patterned top electrode, the polymer liquid grows upwards firstly under the protrusions of the top electrode due to the higher electric field causing a greater electrostatic force as shown in Fig. 3(b). The growing polymer touches the protrusive surface of the top electrode, and is stopped from moving further upwards (Fig. 3(c)). The liquid continues to flow upwards and converges at the top, achieving the replication of the top electrode (Fig. 3(d)). The simulation results show that nanochannels with a width of around 25 nm (full-width at half-maximum) and a depth of 50 nm can be successfully achieved. As the ridge between the channels has a width of 28 nm a microstructure with an aspect ratio of larger than 1.5 : 1 can be obtained by this method. Fig. 4 shows how the voltage distribution and electric field change of one period during the nanostructures evolution change over time. The deflection of the field lines at the interface is caused by the change of the dielectric of the materials.

The model can be used to determine the period limit L_P as shown in Fig. 5. The width and the height of the electrode protrusions are both 20 nm. The initial film thickness is 30 nm and the gap between the film surface and the bottom of the electrode protrusions is 50 nm. A voltage of 70 V is applied to the top electrode. The only changing parameter is the spacing between the adjacent electrode protrusions. As shown in Fig. 5(c), the fabrication limit is reached when the spacing of the electrode protrusions is 85 nm, that is, the minimum nanochannel with a width of around 85 nm is obtained. If the spacing is smaller than the critical value of 85 nm, channels with the same depth cannot be formed as shown in Fig. 5(a) or Fig. 5(b). In general, when reaching the fabrication limit, the width of the two polymeric columns on the outer sides is slightly larger than that of the inner ones. In other words, the width of the channels on the outer sides is smaller (70 nm) than that of the intermediate channel (80 nm). Above that limit, the three nanochannels are identical with a width of 81 nm as shown in Fig. 5(d).

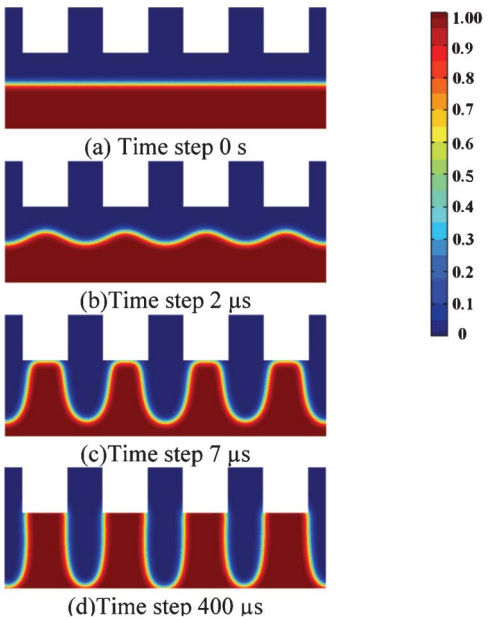

Fig. 3 Spatiotemporal evolution of a 30 nm thick polymer liquid interface. Red color represents the polymer liquid, and the blue represents air.

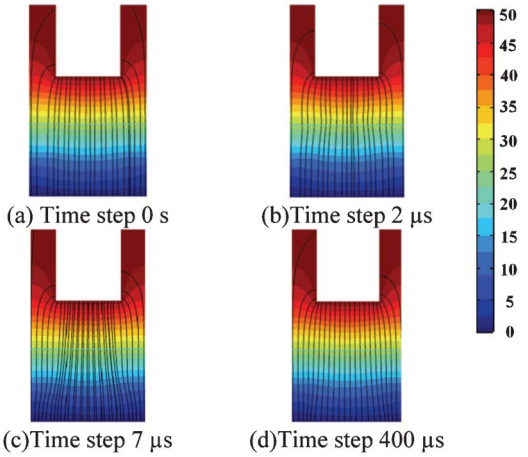

Fig. 4 Evolution of the voltage (color) and electric field (black lines) of one period at various time steps. Dimension unit is nm.

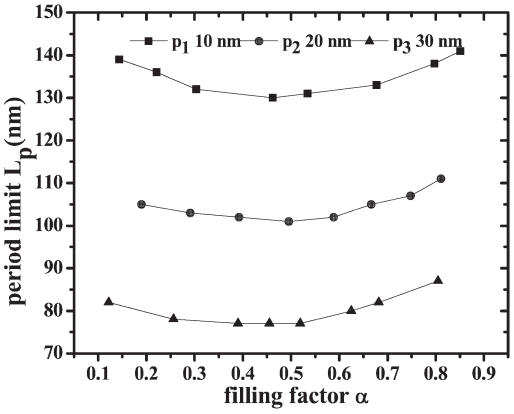

Fig. 6 The period limit L_P *versus* the filling factor α under different heights of the electrode protrusions *p*. p_1, p_2 and p_3, correspond to the height of the electrode protrusions and are 10 nm, 20 nm and 30 nm, respectively. d = 100 nm, ψ_{up} = 70 V, h_0 = 30 nm.

The period limit of the nanochannels, L_P, that is the width of the electrode protrusions plus the critical value of the spacing between the adjacent electrode protrusions, is 105 nm in this example. Based on such a method, we investigate how parameters such as the filling factor α, defined as the ratio of the width to the period limit of the electrode protrusions, the aspect ratio β, defined as the ratio of the width to the height of the electrode protrusions, the applied voltage ψ_{up}, the film thickness h_0 and the electrode spacing d affect the period limit L_P.

The influence of the filling factor

Fig. 6 shows the relationship between L_P and the filling factor α under different heights of electrode protrusions p. For the example above, periodic structures can only be obtained if the filling factor $\alpha \leqslant 0.19$. If the width of the electrode protrusions is 30 nm, the filling factor corresponding to the period limit becomes 0.29. In other words, Fig. 6 not only displays the critical filling factor corresponding to the period limit but also demonstrates its variation with the width of the electrode protrusions. The change of the filling factor α from 0.1 to 0.9 is achieved by increasing the width of the electrode protrusions w. The electrode spacing is fixed at 100 nm. The initial film thickness h_0 is 30 nm, and the applied voltage ψ_{up} is 70 V. The parameters p_1, p_2 and p_3, corresponding to the heights of the electrode protrusions, are 10 nm, 20 nm, and 30 nm, respectively. The lowest period limit L_P of 77 nm is obtained for the largest height of the electrode protrusions with a filling factor of around 0.5, namely, the lowest period can been obtained when the width of the electrode protrusion is 35 nm. In general, the larger the height of the electrode protrusions, the smaller the period limit. To achieve the minimum period for the nanochannels, the electrode should have a large aspect ratio and a filling factor of around 0.5.

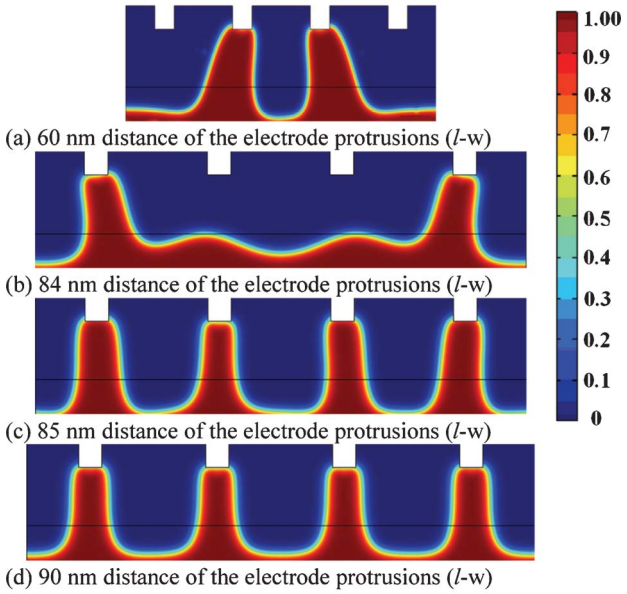

Fig. 5 The final nanofluidic channels induced by an electric field with different separations of the electrode protrusions (*l*–*w*). The red color represents the viscous polymer, and blue represents air. Dimension unit is nm.

The influence of the aspect ratio

Fig. 7 shows the relationship between the period limit L_P and the aspect ratio β for different heights of the electrode protrusions p. The electrode spacing d is 100 nm. The initial film thickness h_0 is 30 nm and the applied voltage ψ_{up} is 70 V. p_1, p_2 and p_3, are 10 nm, 20 nm, and 30 nm, respectively. The lowest period limit is 77 nm when the height of the electrode protrusion is 30 nm and the aspect ratio is 0.857, corresponding to a nanochannel with a width of around 42 nm. The depth of the nanochannel is 70 nm. However, there is not enough film to form the polymeric columns with a width as that of the electrode protrusion (27 nm for the inner columns). Generally, increasing the height of the electrode protrusions can provide a relatively smaller period limit. However different heights of electrode protrusions provide different optimum aspect ratios, which are 0.2, 0.4 and 0.8 for heights of 10 nm, 20 nm and 30 nm, respectively.

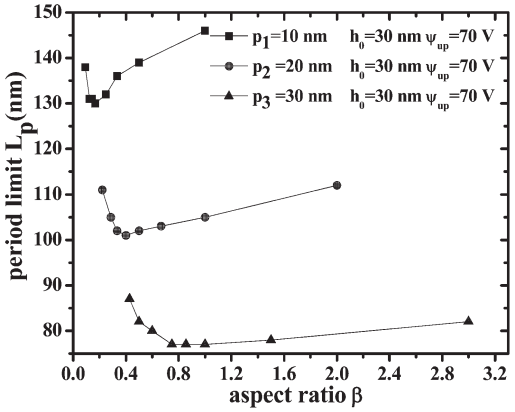

Fig. 7 The period limit L_P changes with aspect ratio β for different heights of electrode protrusions. p_1, p_2 and p_3 correspond to the height of the protrusion and are 10 nm, 20 nm and 30 nm, respectively. d = 100 nm, ψ_{up} = 70 V, h_0 = 30 nm.

The influence of the applied voltage

Fig. 8 shows the relationship of the period limit L_P against the applied voltage ψ_{up}. L_P decreases with an increasing applied voltage. The smallest period is 68 nm for electrode protrusions with a width of 30 nm and a height of 30 nm when a voltage of 80 V is applied. The smallest outer channels are 38 nm wide, the intermediate is 48 nm wide and a 70 nm depth can be obtained.

The influence of the initial film thickness

Fig. 9 shows the relationship of L_P *versus* h_0. The smallest period obtained is 64 nm when the electrode protrusion has a width of 30 nm and a height of 30 nm. The smallest channel width obtained is just 30 nm and the intermediate channel is 38 nm wide. The depth of the nanochannel is 70 nm. In general, the period becomes small when the initial film thickness increases.

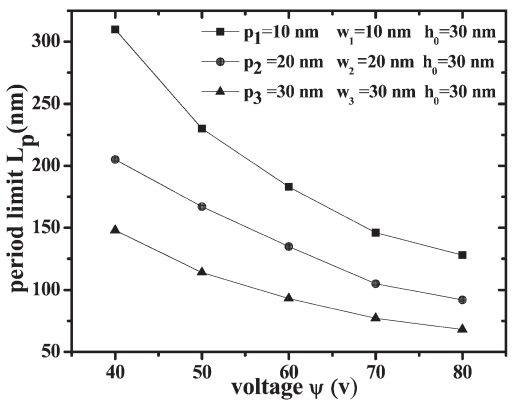

Fig. 8 The dependence of the period limit L_P on the applied voltage ψ_{up} for the cases where w = 10 nm, 20 nm, 30 nm and p = 10 nm, 20 nm, 30 nm. h_0 = 30 nm and d = 100 nm.

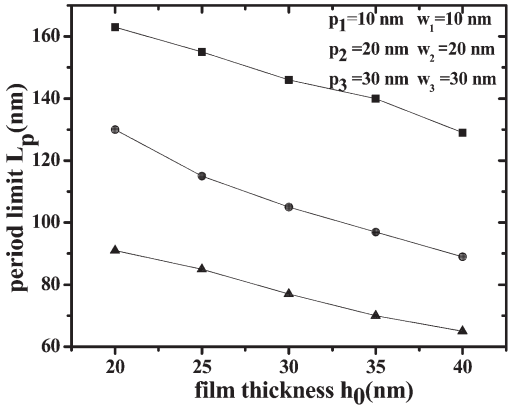

Fig. 9 The variation of the period limit L_P with the film thickness h_0 for the case where ψ_{up} = 70 V, and d = 100 nm.

The influence of the electrode spacing

Fig. 10 shows the variation of L_P against the electrode spacing d. The smallest period is 53 nm when the electrode spacing is 80 nm and the electrode protrusion has a width of 30 nm and a height of 30 nm. The smallest channel has a width of only 25 nm, the intermediate channel has a width around 25 nm and a 50 nm depth. In general, the smaller the electrode spacing, the smaller the period.

Conclusions

In this paper, the finite element numerical analysis method has been employed to study the fabrication limit of polymeric nanochannels using the electrical field induced method. It is shown that, by applying an external heterogeneous electrical field, polymeric nanochannels with a width of 25 nm and a depth of 50 nm can be produced. In addition, the fabrication limit on the period of the nanochannels has been characterised as a function of the filling factor, the aspect ratio of the electrode protrusion, the electrode spacing, the initial film

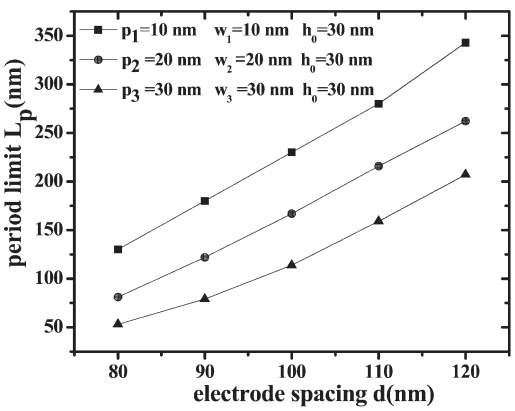

Fig. 10 Period limit L_P against the electrode spacing d when ψ_{up} = 50 V and h_0 = 30 nm.

thickness and the applied voltage. The optimum conditions to obtain the minimum nanochannels have been obtained. These results are to provide essential guidance for the fabrication of those nanochannels for applications covering nanofluidics or nanophotonics.

Acknowledgements

The authors acknowledge the financial support from the National Natural Science Foundation of China with grant numbers 90923036 and 60977041 as well as the 100 Talents Program of Chinese Academy of Sciences. Financial contribution from the British Engineering and Physical Sciences Research Council (EPSRC) through the IeMRc flagship project entitled SMART MICROSYSTEMS is also acknowledged.

Notes and references

1 G. Reiter, *Langmuir*, 1993, **9**, 1344–1351.
2 P. G. D. Gennes, *Rev. Mod. Phys.*, 1985, **57**, 827–863.
3 R. Y. Rozen, T. Kerle and J. Klein, *Science*, 1999, **285**, 1254–1256.
4 A. Sharma, *Langmuir*, 1993, **9**, 861–869.
5 K. Kargupa and A. Sharma, *Langmuir*, 2002, **18**, 1893–1903.
6 S. Herminghaus, K. Jacobs, K. Mecke, J. Bischof, A. Fery, M. I. Elhaj and S. Schlagowski, *Science*, 1998, **282**, 916–919.
7 A. Vrij and J. Overbeek, *J. Am. Chem. Soc.*, 1968, **90**, 3074–3078.
8 A. Gonzalez and A. Castellanos, *Phys. Rev.*, 1996, **53**, 3573–3578.
9 D. Tseluiko, M. G. Blyth, D. T. Papagergiou and J. M. V. Broeck, *J. Eng. Math.*, 2010, **68**, 339–353.
10 H. Kim and S. G. Bankoff, *Phys. Fluids A*, 1992, **4**, 2117–2130.
11 B. Uma and R. Usha, *Phys. Fluids*, 2008, **20**, 032102.
12 D. Tseluiko, M. G. Blyth, D. T. Papageorgiou and J. M. V. Broeck, *Phys. Fluids*, 2008, **20**, 042103.
13 D. Tseluiko, M. G. Blyth, D. T. Papageorgiou and J. M. V. Broeck, *J. Fluid Mech.*, 2008, **597**, 449–475.
14 V. Shankar and A. Sharma, *J. Colloid Interface Sci.*, 2004, **274**, 294–308.
15 M. F. E. Sayed, M. H. M. Moussa, A. A. A. Hassan and N. M. Hafez, *Appl. Math.,* Volume 2011, Article ID 498718, 35 pages.
16 Z. Lin, T. Kerle, S. M. Baker and D. A. Hoagland, *J. Chem. Phys.*, 2001, **114**, 2377–2381.
17 S. Y. Chou and L. Zhuang, *J. Vac. Sci. Technol., B*, 1999, **17**, 3197–3202.
18 E. Schäffer, T. T. Albrecht, T. P. Russell and U. Steiner, *Nature*, 2000, **403**, 874–877.
19 E. Schäffer, T. T. Albrecht, T. P. Russel and U. Steiner, *Europhys. Lett.*, 2001, **53**, 518–524.
20 D. Kim and W. Lu, *Comput. Mater. Sci.*, 2006, **38**, 418–425.
21 L. F. Pease and W. B. Russel, *Langmuir*, 2004, **20**, 795–804.
22 A. Esmaeeli and M. N. Reddy, *Int. J. Multiphase Flow*, 2011, **37**, 1331–1347.
23 N. Wu and W. B. Russel, *Nano Today*, 2009, **4**, 180–192.
24 R. V. Craster and O. K. Matar, *Phys. Fluids*, 2005, **17**, 032104.
25 L. F. Pease and W. B. Russel, *J. Non-Newtonian Fluid Mech.*, 2002, **102**, 233–250.
26 L. F. Pease and W. B. Russel, *J. Chem. Phys.*, 2003, **118**, 3790–3803.
27 P. S. G. Pattader, I. Banerjee, A. Sharma and D. Bandyopadhyay, *Adv. Funct. Mater.*, 2011, **21**, 324–335.
28 Z. Lin, T. Kerle and T. P. Russell, *Macromolecules*, 2002, **35**, 3971–3976.
29 T. P. Russell, Z. Lin, E. Schäffer and U. Steiner, *Fibers Polym.*, 2003, **4**, 1–7.
30 D. Du and D. Srolovitz, *Appl. Phys. Lett.*, 2004, **85**, 4917–4919.
31 N. Wu and W. B. Russel, *Ind. Eng. Chem. Res.*, 2006, **45**, 5455–5465.
32 G. Tomar, V. Shankar, A. Sharma and G. Biswas, *J. Non-Newtonian Fluid Mech.*, 2007, **143**, 120–130.
33 J. Sarkar, A. Sharma and V. B. Shenoy, *Phys. Rev. E: Stat., Nonlinear, Soft Matter Phys.*, 2008, **77**, 031604.
34 D. Bandyopadhyay, A. Sharma, U. Thiele and P. D. S. Reddy, *Langmuir*, 2009, **25**, 9108–9118.
35 S. Srivastava, P. D. S. Reddy, C. Wang, D. Bandyopadhyay and A. Sharma, *J. Chem. Phys.*, 2010, **132**, 174703.
36 E. M. Tian, T. P. Svobodny and J. D. Philips, *Applied Mathematics and Mechanics*, 2011, **32**, 1039–1046.
37 N. Wu, L. F. Pease and W. B. Russel, *Langmuir*, 2005, **21**, 12290–12302.
38 R. Verma, A. Sharma, K. Kargupta and J. Bhaumik, *Langmuir*, 2005, **21**, 3710–3721.
39 A. Atta, D. G. Crawford, C. R. Koch and S. Bhattacharjee, *Langmuir*, 2011, **27**, 12472–12485.
40 H. Chen, W. Yu, S. Cargill, M. K. Patel, C. Bailey, C. Tonry and M. P. Y. Desmulliez, *Microfluid. Nanofluid.*, 2012, **13**, 75–82.
41 S. Y. Chou, L. Zhuang and L. Guo, *Appl. Phys. Lett.*, 1999, **75**, 1004–1006.
42 A. Onuki, *Phys. A*, 1995, **217**, 38–52.
43 H. K. Yeoh, Qi Xu and O. A. Basaran, *Phys. Fluids*, 2007, **19**, 114111.
44 Q. Yang, B. Q. Li and Y. Ding, *Soft Matter*, 2013, **9**, 3412–3423.
45 M. Sussman, P. Smereka and S. Osher, *J. Comput. Phys.*, 1994, **114**, 146–159.
46 Y. C. Chang, T. Y. Hou, B. Merriman and S. Osher, *J. Comput. Phys.*, 1996, **124**, 449–464.